Pumping Rate and Surface Morphology Dependence of Ionization Processes in Matrix-Assisted Laser Desorption Ionization

Yong Chen and Akos Vertes*

Department of Chemistry, The George Washington University, 725 21st Street, N.W., Washington, D.C. 20052

Received: June 27, 2003; In Final Form: September 10, 2003

The quantitative photophysical description of matrix-assisted laser desorption ionization (MALDI) is explored by using a wide range of optical pumping rates established by 22 ps and 4 ns laser pulse lengths. Furthermore, the sample morphology dependence of ionization was tested on pellets compacted at different pressures, yielding surfaces of varying roughness. Mass spectra acquired from 2,5-dihydroxybenzoic acid pellets showed an increase in the matrix ionization threshold fluence with increasing pressure during pellet formation. Sample surfaces produced at higher pressure exhibited lower fractal dimension. This fractal coarsening is suggested to be behind the elevated ion formation threshold in these samples. Compared with conventional nanosecond pulses, the ionization threshold values were consistently higher by a factor of ~2 for the picosecond laser. The DHB matrix was dramatically more likely to yield fragment ions when irradiated with the longer laser pulse, indicating significant differences in the primary ionization mechanism. Furthermore, fragmentation escalated with the increase in laser fluence for both lasers, although this effect was significantly more pronounced for nanosecond pulses. Dried droplet samples of sinapinic acid and α-cyano-4-hydroxycinnamic acid also showed higher fragmentation with the longer laser pulse. Different optical pumping rates and relaxation channels are thought to be responsible for the significant difference in the yield of matrix molecular ions. For small analytes (≤2000 Da), molecular ion signal was easily acquired with both lasers, whereas for large molecules (≥5000 Da), the analyte ion yield was low or even vanishing with the picosecond laser. The nanosecond laser produced ions from the small and large analytes with comparable yields. These observations are compatible with the assumption that the longer laser pulse can sequentially desorb and ionize analyte molecules due to the extended interaction of the laser pulse and the MALDI plume, whereas the shorter pulse can only desorb the analyte molecules but cannot promote their ionization due to its limited temporal overlap with the plume.

Introduction

Due to its ability to produce intact gas-phase molecular ions, matrix-assisted laser desorption ionization (MALDI) mass spectrometry has evolved into an established technique for biomolecular and macromolecular analysis.[1−3] Recent advances in the kinetic description of matrix ionization emphasize the influence of subnanosecond photophysical processes on the MALDI ionization mechanism.[4−6] The most elaborate model accounts for excitation, radiative and nonradiative relaxation, and $S_1 + S_1$ and $S_1 + S_n$ pooling resulting in ion formation.[6] Gas dynamic effects are introduced through a similarity model, whereas analyte ion formation is driven by a matrix-to-analyte charge-transfer reaction.[7] These models are based on widespread observations but only on limited quantitative time-dependent ion yield data.[8−10] Although many of the MALDI phenomena are correctly reproduced by the models (e.g., matrix suppression effects), some experimentally obvious processes, such as matrix fragmentation, are absent from all of them. Competition between excitation, relaxation, fragmentation, and other dissipation processes can be probed by changing the pumping rate through the introduction of significantly shorter laser pulses.

Ionization in MALDI is considered to be the result of two major processes: primary ions (e.g., matrix ions) are generated during or shortly after the laser pulse and secondary ions (e.g., analyte ions) are produced via cation (mostly proton) transfer reactions in the expanding plume. The four prominent primary ion formation mechanisms designate the source of these ions as excited-state proton transfer, exciton pooling, intracluster proton transfer, and matrix disproportionation that become dominant at different stages and time scales during the plume development process.[11] As long as energy deposition outpaces dissipation by heat conduction in the solid, these ionization processes are dependent on laser fluence rather than on irradiance.[12−16] As a result, primary and secondary ion signals emerge when the fluence exceeds the corresponding thresholds.

To explore the effect of pumping rate, early experiments were performed with lasers of vastly different pulse durations (3 ns vs 560 fs in ref 14). In that study, the predominance of a fluence threshold for ion generation was confirmed. More recently, MALDI results with fast pulses both in UV and in IR showed negligible differences between analyte mass spectra for the laser parameters tested.[17] On this basis, the authors concluded that mass spectra in themselves were not sufficient to uncover the operative MALDI mechanism.[17] However, marked differences do exist between MALDI mass spectra taken with the nanosecond and femtosecond pulses. Most remarkably, Demirev et al. found that the yield of detected insulin ions in femtosecond MALDI was significantly lower than that in the nanosecond

* Address correspondence to this author. E-mail: vertes@gwu.edu. Phone: (202) 994-2717. Fax: (202) 994-5873.

10.1021/jp035844u CCC: $25.00
Published on Web 10/25/2003

domain and that the femtosecond laser was unable to produce protein ions with masses higher than insulin.[14]

Pumping rate studies in multiphoton ionization showed that the length of the laser pulse had a direct influence on the mechanism of ionization.[18,19] The product yields of multiphoton ionization and dissociation can be explained by two competing mechanisms. In the ladder-switching mode, the unimolecular dissociation successfully competes with the optical pumping, thus the excited molecule breaks up into fragments before it reaches the ionization potential (IP). The excitation ladder switches from the molecule to the fragment product for further photon absorption. In the ladder-climbing mode, the optical pumping rate is very high (e.g., in the case of femtosecond pulse length), and the absorbing species can be consecutively excited up to its IP to form molecular ions. In this case, fragmentation is due to the excess energy of the ion. Analogous to these mechanistic steps, different matrix ionization pathways are expected in MALDI when lasers of very different pulse length are used. This competition between ionization and fragmentation has a significant influence on primary ionization that is considered critical in MALDI.[11] Furthermore, by extending the existing models to include ladder switching the formation of ubiquitous matrix fragment ions can be mechanistically explained.

Desorption processes initiated by ultraviolet lasers have been successfully described by hydrodynamic models[20] and by molecular dynamics calculations.[21−26] In these studies, laser energy is assumed to be deposited into the sample during the laser pulse, and the desorption process ensues on a subnanosecond time scale with guest and matrix molecules ejected into the gas phase. Phase transition in the top layers of the matrix was observed at ~60 ps after the onset of laser heating.[26] These models successfully explain many observations in MALDI induced by lasers of nanosecond pulse length. However, to explore the fast energy deposition processes inherent in these models, experiments with lasers of much shorter pulse length (low picosecond range) are needed.

Sample morphology has been recognized as a key factor that affects the ionization threshold and the stability of the MALDI signal.[27−29] The commonly used dried droplet (DD) method gives rise to highly inhomogeneous lognormal crystal size distributions.[29] When exposed to laser radiation, the small (submicron) crystals can be depleted, and as a consequence, the ion signal rapidly decays. To desorb and ionize from larger crystals, higher laser intensity is needed.[29] Although this effect is commonly observed, due to the difficulty of controlling sample morphology, quantitative results are not available. In this study, we systematically change the sample morphology by producing pressed pellet samples at different pressures. Matrix ion yield measurements on these samples provide insight into the effect of morphology on MALDI.

To explore the effect of pumping rate in the picosecond pulse length domain in MALDI, we used lasers with 22 ps and 4 ns pulse length. This enabled us to compare ionization processes in these time domains in pure matrix and analyte/matrix samples. Pressed pellets of the pure matrix were used for three reasons: (a) to avoid the uneven distribution of matrix crystals in space and size as encountered in DD samples; (b) to provide sufficient material for continuous and steady ion signal; and (c) to systematically explore the effect of sample morphology on ion yields. As shown in the two-pulse experiments,[8−10] to account for the dynamic behavior of the interaction volume, it is important to explore the various energy dissipation mechanisms including the relaxation processes involved. The comparison of laser excitation with different pulse lengths promises insight into fast dynamics in MALDI.

Experimental Section

Instrumentation. A home-built linear time-of-flight mass spectrometer (TOF-MS) (based on TOF-101, Comstock Inc., Oak Ridge, TN) was equipped with a laser ionization source. A detailed description of the instrument can be found elsewhere.[30] A nitrogen laser emitting at 337 nm (VSL-337ND, Laser Science Inc., Newton, MA) was triggered at 2 Hz to deliver 4-ns pulses. A mode-locked $3\times\omega$ Nd:YAG laser (PL2143, EKSPLA, Vilnius, Lithuania) was customized by the manufacturer to fire at 2 Hz and the harmonic generators were adjusted to accommodate the change in thermal load. To reject the residue from the 532-nm second harmonic in the 355-nm output, a low-pass optical filter with transmission >90% at 355 nm and <3% at 532 nm (10SWF-500, Newport Corp., Irvine, CA,) was implemented. As the residual 532-nm radiation was extremely weak, it did not play an appreciable role in the MALDI process even without filtering. The energy of the 22-ps pulses was adjusted with a variable attenuator (935-5-OPT, Newport, Fountain Valley, CA), and a 2.5-mm-diameter aperture was used to limit the beam profile. To maintain the beam profile, the variable attenuator changes its transmission by changing the Fresnel reflection angle on two pairs of wedged optical plates. Individual pulse energies, ranging from 1 to 10 μJ, were measured with a pyroelectric joule meter (Model J4-05, Molectron, Portland, OR). The laser beam was focused onto the stainless steel probe at a 45° angle. The focal areas were determined by measuring the burn marks on photographic paper under a microscope-mounted CCD imaging system. A detailed description of the imaging system can be found elsewhere.[29] Due to the inclination of the beam, elliptical spots of (93×97) μm^2 and at (53×57) μm^2 were produced by the nanosecond and the picosecond laser, respectively. The generated ions were extracted by 25-kV accelerating voltage into a 2.1-m effective-length flight tube. A 25-mm-diameter dual microchannel plate (30293, Burle Electrooptics Corp., Sturbridge, MA) chevron assembly was biased to −1.7 kV for the detection of ions. After amplification (9305, EG&G, Oak Ridge, TN), a 1.5-GHz digital oscilloscope (LC684DXL, LeCroy, Chestnut Ridge, NY) was used to capture individual spectra at a 200-MS/s sampling rate. The reduced sampling rate allowed increased spectrum acquisition rates without compromising peak area determination by undersampling. To explore the sample morphology at the submicrometer level, a scanning electron microscope (SEM) (Hitachi S-2400, Nissei Sangyo, Gaithersburg, MD) was used.

Materials. The matrixes, 2,5-dihydroxybenzoic acid (DHB), sinapinic acid (SA), and α-cyano-4-hydroxycinnamic acid (CHCA), as well as the analytes, such as leucine enkephalin, human angiotensin I, substance P, bovine insulin, cytochrome C, lysozyme, superoxidase dismutase, and bovine serum albumin, were obtained from Sigma Chemical Co. (St. Louis, MO). Acetonitrile solvent (HPLC grade) was purchased from Fisher Scientific (Springfield, NJ), and deionized water (18.2 MΩ·cm) was produced by using an E-pure system (Barnstead, Dubuque, IA). Trifluoroacetic acid (reagent grade) was obtained from Aldrich (Milwaukee, WI).

Sample Preparation. Before use, the DHB matrix was recrystallized in pure acetonitrile and was ground with a mortar and pestle. For the pressed pellet samples, a die, designed to prepare salt windows for IR spectroscopy, was used. To systematically change the surface morphology, the press was set to different pressures (100, 200, and 300 MPa, i.e., 15 000,

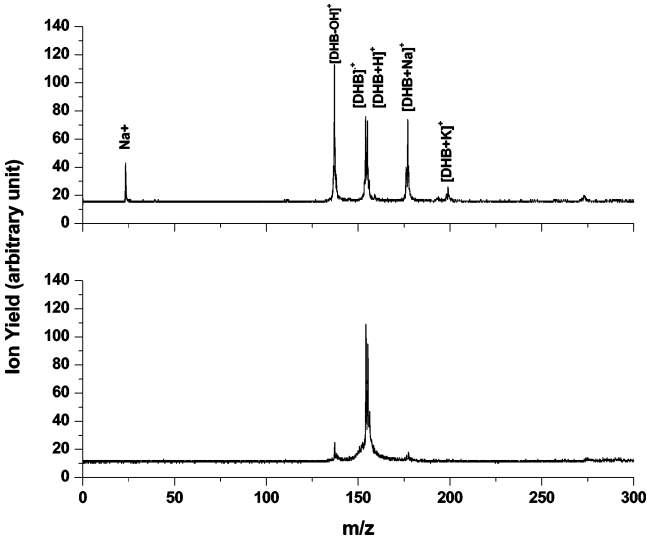

Figure 1. MALDI mass spectra from a DHB pellet measured with the nanosecond laser (top panel) and with the picosecond laser (bottom panel).

29 000, and 44 000 psi, respectively) and ~0.1 mm thick pellets were obtained by pressing ~30 mg of DHB powder for 30 s. For the MALDI experiments, a section (~3 × 3 mm^2) of the pellet was attached to the stainless steel probe tip with double-sided tape. Pellet sections for the SEM images were attached to the sample stage with conductive silver paste and sputter coated with gold−palladium to ensure a conductive surface with no change to the surface morphology.

Analyte solutions were prepared at ~5×10^{-4} M concentration in 0.1% TFA, whereas the saturated solutions of DHB, SA, and CHCA were prepared in 70% acetonitrile. For the DD preparation, 2 μL of the analyte solution was mixed with 2 μL of DHB solution to obtain a mixture with an ~3000:1 matrix/analyte molar ratio and 2 μL of this mixture was air-dried on the stainless steel probe at room temperature. The DD samples of neat DHB, SA, and CHCA were prepared by air-drying 2 μL of their respective saturated solutions on the probe.

Data Acquisition and Processing. For each sample, the minimum laser energy that resulted in the appearance of matrix ion signal was determined. To obtain the fluence dependence of the ion yields, the energy was gradually increased by opening up the attenuator. Typically, 10 individual spectra were averaged and 10−15 averaged spectra were acquired at each laser energy level. The energy was measured for each set of data and converted into fluence. Data processing was carried out with custom written software on a LabVIEW platform (Version 6.0, National Instruments, Austin, TX). The ion peaks of interest were integrated in time for the comparison of ion yields.

For pellet samples, SEM images of the surface were acquired at 15 kV with 500× magnification and at 25 kV with 15 000× magnification. The fractal dimensions of the SEM images for each pellet were calculated by analyzing the thresholded 15 000× images with the box-counting algorithm utilizing the HarFA fractal analysis package (obtained from http://www.fch.vutbr.cz/lectures/imagesci/). For each box size, r, the number of boxes containing both black and white pixels, $N(r)$, was counted. The fractal dimension was calculated as the slope of the linear region in the $\ln(N)$ vs $-\ln(r)$ plot.

Results and Discussion

Total Yield of Matrix Ions. Consistent with earlier observations, the signal from DHB pellets was more stable and more persistent than that from neat DD samples.[9] Initially, mass spectra were acquired with both lasers on neat DHB pellets as a function of laser fluence. More than 100 spectra were acquired on a single spot at each fluence level without apparent signal decay. To compare the pressed pellet method with typical MALDI preparations, DD samples were also studied. On these samples, ion signal decay often occurred during the first 20−30 shots, thus several spots had to be tested with the same laser fluence to obtain 4−5 averaged spectra.

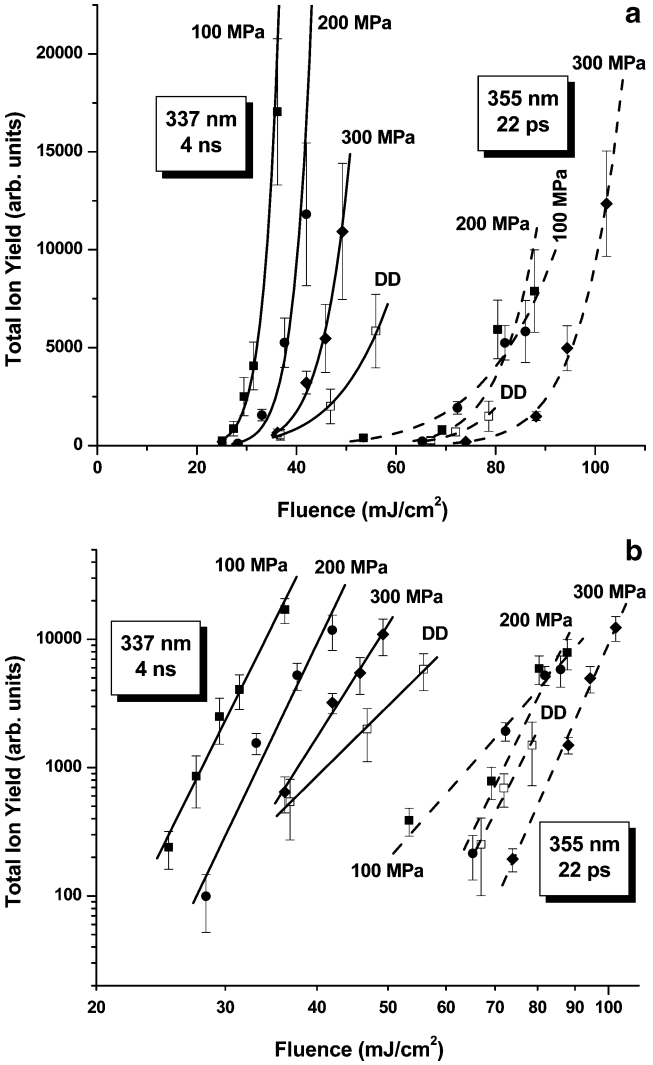

Figure 2. (a) Linear fluence-dependence of total ion yields (fragment and molecular ions) of DHB pellets made with 100 (■), 200 (●), and 300 MPa (◆) pressures and of DD samples (□) measured with the nanosecond laser (solid line) and the picosecond laser (dash line). (b) Logarithmic fluence-dependence of total ion yields (fragment and molecular ions) of DHB pellets made with 100 (■), 200 (●), and 300 MPa (◆) pressures and of DD samples (□) measured with the nanosecond laser (solid line) and picosecond laser (dashed line).

With the nitrogen laser, several ion species were obtained from pure DHB matrix, such as DHB radical cation ($M^{\bullet+}$, m/z 154), deprotonated and protonated DHB ions ($(M - H)^+$, $(M + H)^+$, and $(M + 2H)^+$, m/z 153, 155, and 156, respectively), dehydroxylated DHB ion ($(M + H - H_2O)^+$ or $(M - OH)^+$, m/z 137), and sometimes alkalinated DHB ions ($(M + Na)^+$ and $(M + K)^+$, m/z 177 and 193, respectively) (see the top panel of Figure 1). The formation pathways of these ions were described in ref 31. All of these ion peaks were integrated to provide the total ion yield of DHB in the MALDI process. In agreement with other studies utilizing nitrogen laser, the relative

TABLE 1: Exponents, *B*, and Regression Coefficients, *R*, for Total Ion Yield, *Y*, versus Laser Fluence, *F*, Relationship, $Y \propto F^B$, for Pressed Pellet Samples of DHB Prepared at Different Pressures Compared to More Conventional DD Samples

	nitrogen laser				mode locked 3×ω Nd:YAG laser			
parameter	DD	100 MPa	200 MPa	300 MPa	DD	100 MPa	200 MPa	300 MPa
B	5.7 ± 0.2	11.3 ± 0.7	10.2 ± 1.9	8.9 ± 1.0	10.4 ± 2.1	6.4 ± 1.4	9.6 ± 2.7	13.0 ± 0.8
R	1.00	0.99	0.97	0.99	0.98	0.95	0.93	1.00

yield of alkalinated species decreased as laser power increased (not shown). Although it was not analyzed quantitatively, the radical-to-protonated cation ratio appeared to be stable throughout the studied laser fluence range. As a comparison, the bottom panel in Figure 1 shows the MALDI mass spectra from DHB pellets with use of the mode locked 3×ω Nd:YAG laser. Clearly, this spectrum shows significantly less dehydroxylation and negligible alkalination than the one in the top panel. The lack of alkalination is probably due to the significantly higher irradiance of the picosecond laser. This is consistent with the observation of declining alkaline ion adduction at increased nitrogen laser fluence (and irradiance).

Figure 2a shows the fluence dependence of the total ion yield for pellets produced at different pressures and for DD samples. The DHB total ion yield curves acquired with a particular laser for DD samples and pellets are grouped together, illustrating that the ionization processes for these samples are also similar in terms of threshold fluence and ion yield. It is interesting to compare Figure 2a with Figure 9 of ref 6. There is quite a good agreement in the qualitative features of our data and the predictions of the photophysical model described in ref 6. In both cases, the 4 ns laser pulse at 337 nm gives lower threshold in ion yield and both lasers produce a power law behavior. The measured threshold fluence gap between the two wavelengths is somewhat less than the factor of 7 predicted by the model. This discrepancy originates from the absorption cross-section values used in the model.

Figure 2b shows the log−log representation of the same data. In these variables, the ion yield curves show remarkable linearity, confirming the $Y \propto F^B$ power law relationship, where Y is the total matrix ion yield, F is the fluence, and B is the exponent. Table 1 summarizes the exponents of this relationship and the corresponding R regression coefficients. With the nitrogen laser, the DD sample shows a 6th power dependence that is well below the 10.5 value reported in the literature for the total ion yield.[16] Switching to the mode-locked 3×ω Nd:YAG laser, however, results in much steeper dependence of the total ion yield on fluence ($B = 10.4 \pm 2.1$). To obtain ion yields comparable to that with the nitrogen laser, approximately two times higher fluence is needed. In the case of the nitrogen laser, the needed laser fluence for a given ion yield follows the $F_{100MPa} < F_{200MPa} < F_{300MPa} < F_{DD}$ order. The exponent of the ion yield−fluence relationship increases from ~6 for the DD sample to 9−11 for the pressed pellets. These observations underline the strong morphology dependence of primary ion generation in MALDI. The experiments with the mode-locked laser indicate a less significant difference between the DD samples and pressed pellets. The exponent for DD targets is ~10, whereas the pellets exhibit exponents ranging from 6 to 13.

More systematic changes are observed when the threshold fluence is plotted as a function of the pressure used to prepare the pellets. Figure 3 shows that for both lasers higher pelleting pressure results in higher ionization threshold. For comparison, the ionization threshold for DD samples is also included. It is important to note that these thresholds are slightly higher than the ones reported by other authors, for example the 7 mJ/cm^2 value reported in ref 16. It is not the absolute value of the thresholds, however, that is used in our discussion but the laser fluence to achieve a certain ion yield. This is certainly prudent considering that threshold fluences exhibit significant variations with, e.g., laser spot size.[32]

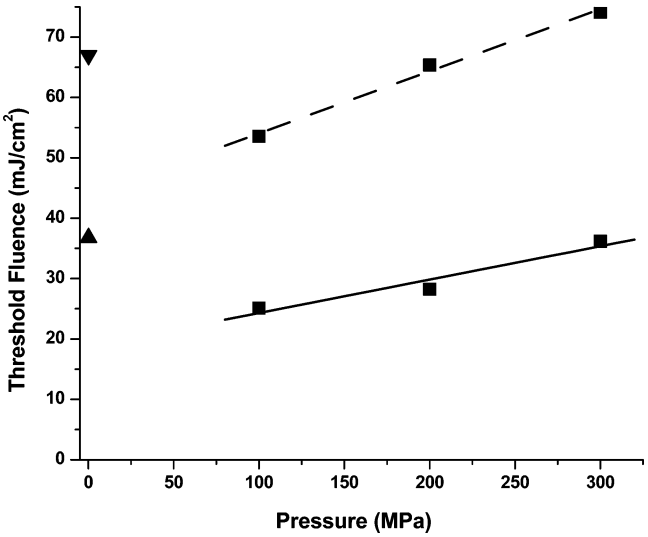

Figure 3. Pressure-dependence of threshold fluence for DHB pressed pellets (■) and for DD samples (nanosecond laser, ▲; picosecond laser, ▼) determined with the nanosecond laser (solid line) and with the picosecond laser (dashed line).

As indicated in ref 29, the size distribution of sample crystallites directly affects the threshold fluence and signal stability. Crystallites that are smaller than a critical size determined by the ability to dissipate energy through heat conduction can be volatized with lower fluence. In this respect, the pressed pellet samples can be viewed as crystallite populations that have been compacted by the high pressure. The surface texture of these samples carries the imprint of the original crystal size distribution. The SEM images in the top panels of Figure 4 show the remarkable changes in surface texture with the increase in compacting pressure. With increasing pressure the small (submicron) features are eliminated, giving rise to a smoother surface with predominantly larger features.

These observations can be quantitatively captured by fractal analysis of the images. Utilizing the HarFA package, the gray scale images are thresholded at 100 level and the fractal dimensions, D, are extracted from the slope of the $\ln(N(r)) = -D \ln(r) + K$ relationship (see bottom panels in Figure 4). The fractal analysis shows a gradual decrease in the fractal dimension of the surface with increasing compacting pressure, reflecting the disappearance of small features and particles. This behavior is known in pressure compacting of powder samples[33] and can be described in more general terms as fractal coarsening of the surface. Disappearance of small features can lead to higher apparent ionization threshold directly through the reduction of the surface area available for desorption and ionization. An alternative explanation, however, can be given by considering the persistence of higher energy density in these small features due to their inability to efficiently dissipate energy through heat conduction.[29] According to this picture, upon laser irradiation

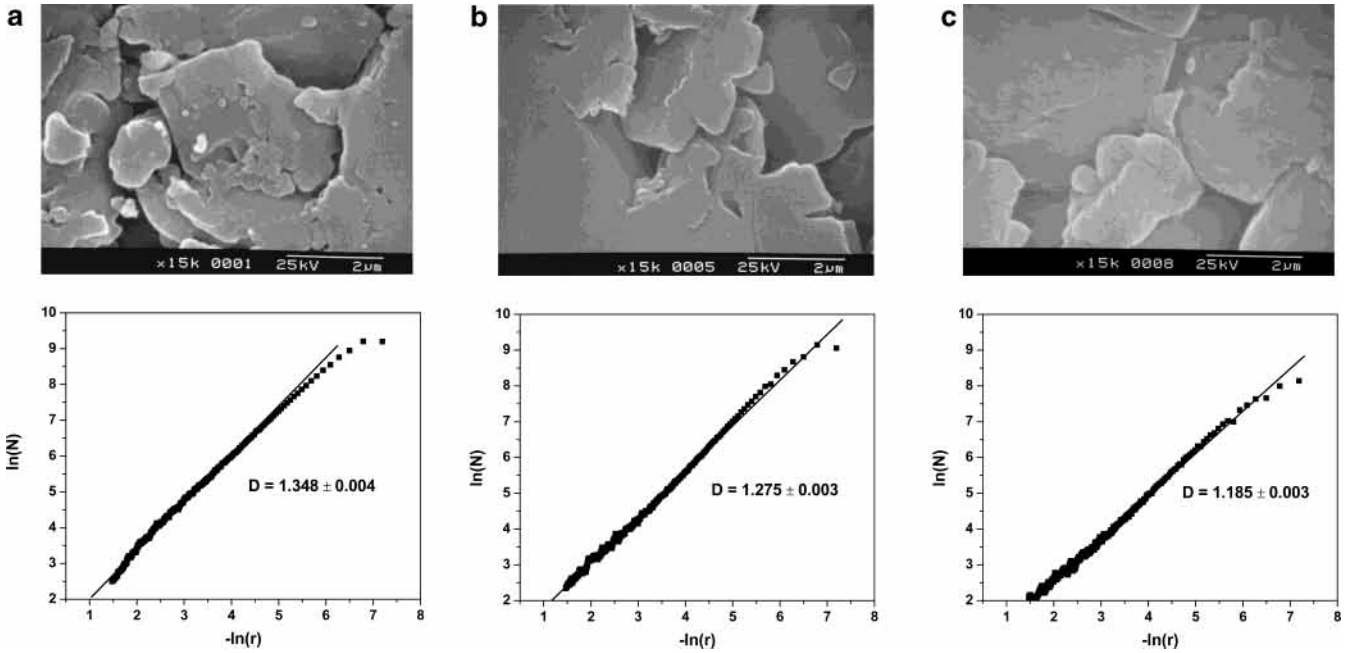

Figure 4. SEM images taken at 15000× magnification (top panels) with fractal dimensions, *D*, extracted from box counting (bottom panels) for pressed pellets made at pressures of (a) 100, (b) 200, and (c) 300 MPa.

of a MALDI sample initially the small (submicron) crystallites are volatilized, eliminating thereby the corresponding part of the crystallite size distribution. This results in a drop in the ion yield that can only be reversed by increasing the laser fluence. This process can be viewed as laser-induced fractal coarsening that has an effect on the ion yield similar to the pressure-induced fractal coarsening demonstrated above. Further testing of this hypothesis by comparing the surface texture before and after laser exposure is underway.

Matrix Fragmentation. Previous studies that focused on guest ion MALDI spectra acquired with laser pulse length ranging from nanosecond to femtosecond showed no apparent difference in the spectra in terms of analyte signal abundance and fragmentation patterns.[14,17] These studies, however, did not address primary ion formation from the matrix. When we compare the mass spectra of pure matrix samples acquired with the nanosecond (Figure 1, top panel) and the picosecond (Figure 1, bottom panel) lasers, it is obvious that significant amounts of DHB fragment and alkali adduct ions are present in the nanosecond spectrum, whereas predominantly DHB molecular ions are produced by the picosecond laser. Similar results are observed with CHCA and SA samples (data not shown).

To illustrate the impact of different pulse lengths and fluences on the production of primary ions, the molecular ion yield, MIY, is defined as:

$$\mathrm{MIY} = \frac{\sum I(\mathrm{M}_i^+)}{\sum I(\mathrm{F}_i^+) + \sum I(\mathrm{M}_i^+)}$$

where $\sum I(M_i^+)$ and $\sum I(F_i^+)$ are the total abundances corresponding to all the (quasi)molecular matrix ions ($M^{\bullet+}$, $[M - H]^+$, $[M + H]^+$, $[M + 2H]^+$, $[M + Na]^+$, and $[M + K]^+$) and all the fragment ions (e.g., $[M - OH]^+$), respectively.

In Figure 5, MIYs of DHB show that larger amounts of molecular ions are generated with the picosecond laser than with the nanosecond laser. The propensity to fragment as the laser fluence increases escalates dramatically for the nanosecond laser, whereas the picosecond laser only induces slightly more fragmentation even when the fluence is far above the threshold

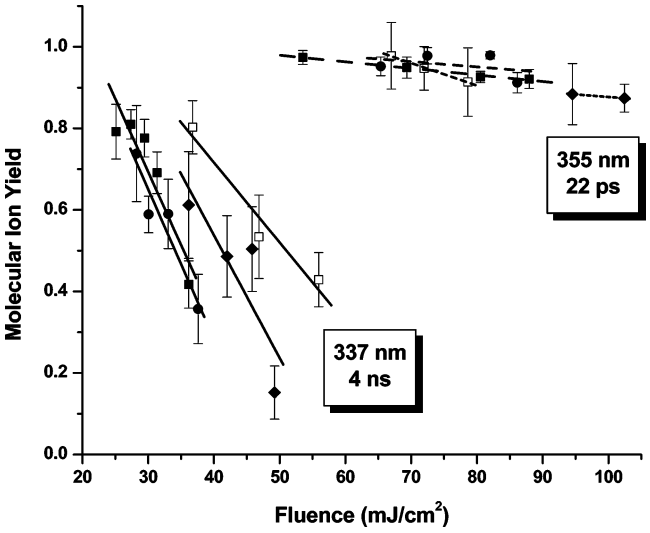

Figure 5. MIYs of DHB pellets made with 100 (■), 200 (●), and 300 MPa (◆) pressure, and of DD samples (□) measured with the nanosecond (solid line) and with the picosecond laser (dash line).

level. Similarly, CHCA and SA consistently show higher molecular ion yields with the picosecond laser (see Figure 6).

The wavelength dependence of the linear absorption coefficient was first examined as the possible source of large MIY variation between the two lasers. However, Dyer and co-workers found no significant difference in the solid-phase absorption coefficients of DHB at 337 and 355 nm, whereas the other two matrixes (CHCA and SA) exhibited higher absorption coefficients at 355 nm than at 337 nm.[4,5] Thus, the spectral variations in the absorption coefficient do not explain the strong dependence of MIYs on laser pulse properties.

The large difference between the pumping rates achieved by the two lasers, however, can be used to explain the variations in MIYs.[18,19] In the case of the picosecond laser, the ionization process is primarily the result of ladder climbing, where the high optical pumping rate exceeds the rate of fragmentation, and the resulting high concentration of excitons leads to efficient pooling and a high yield of molecular ions. This mechanism is

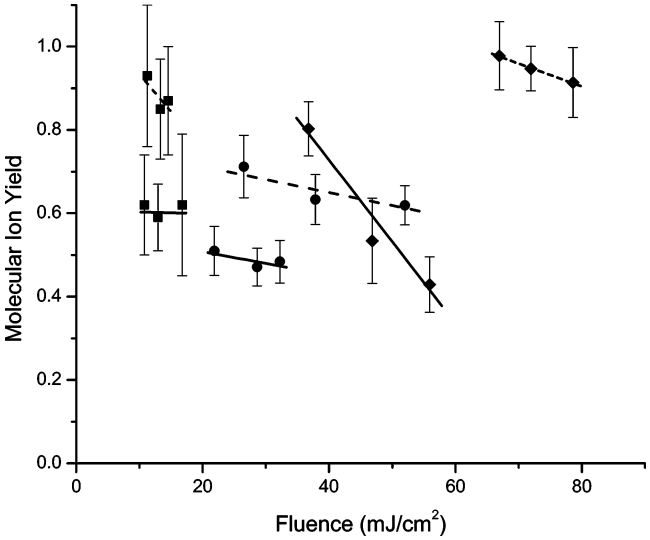

Figure 6. MIYs of DD samples of CHCA (■), SA (●), and DHB (◆) with the nanosecond (solid line) and with the picosecond laser (dash line).

SCHEME 1

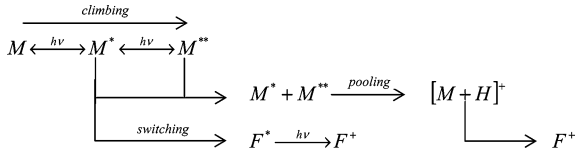

SCHEME 2

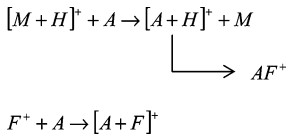

supported by the relatively long singlet lifetime of DHB (0.6 to 1 ns according to refs 36 and 37). At its reduced pumping rate, the nanosecond laser gives rise to a lower concentration of excitons that are likely to pool at a rate comparable to the rate of dissociation into neutral fragments. Thus, on this longer time scale ladder switching competes with ladder climbing resulting in a significant concentration of neutral matrix fragments, F, which can directly absorb a photon to yield fragment ions. These scenarios are depicted in Scheme 1 (electronic excitation is noted by an asterisk).

This mechanism is a natural extension of earlier models, which can be viewed as subsets of Scheme 1 that do not contain the fragmentation channel.[6,7] From Figure 5, it is clear, however, that already at fluences slightly above the ionization threshold nitrogen laser irradiation results in significant matrix fragmentation. As a result, analyte ion formation can proceed along various channels of in-plume ion molecule reactions. In addition to the analytically desirable protonation reaction, the adduction of matrix fragment ions is often observed. Furthermore, the analyte ions can undergo direct fragmentation or metastable decomposition resulting in AF^+ (Scheme 2). The advantage of this model over earlier photophysical descriptions is its direct account for the widespread presence of matrix fragment ions as well as for the formation of a variety of analyte related ions. It is unlikely that neglecting the fragmentation channels can result in a complete account of laser energy deposition or fully describe the fate of matrix molecules.

To describe the ladder-switching step, one must consider the rate of unimolecular decomposition from the excited matrix species, M*, to the F* fragment state. This rate strongly depends on the internal energy of M* stored in the vibrational modes. Similarly, the rates of $[M + H]^+$ decomposition and analyte ion fragmentation depend on their internal energy. Recent studies of internal energy transfer in MALDI indicate that the matrix molecules impart different amounts of internal energy into different analyte ions.[38] The mechanistic steps that are most susceptible to the internal energy content of various species are the unimolecular decomposition reactions leading to F^+ and AF^+ in Schemes 1 and 2. The rate coefficients of these reactions are a very steep function of the internal energy of the precursors, thus, the ion yield curves calculated based on the photophysical model need to be revisited based on the internal energy dependent fragmentation rate coefficients.

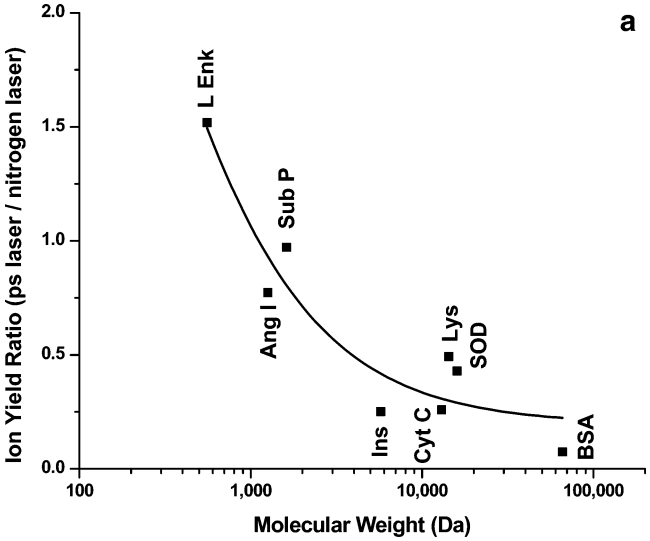

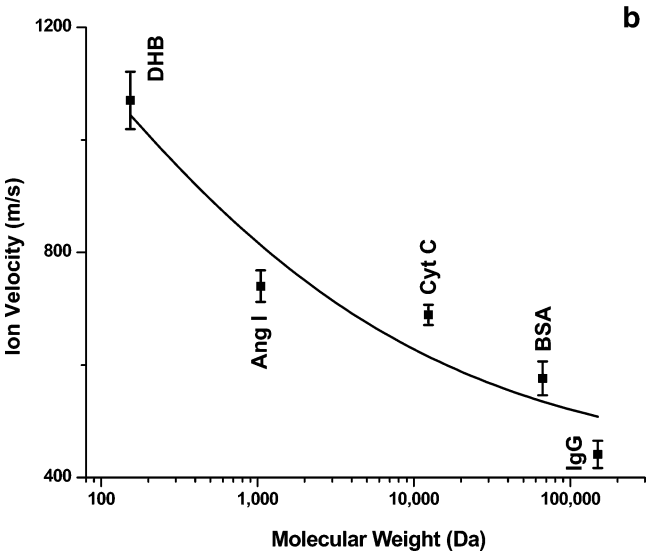

Figure 7. (a) Ratio of analyte ion yields obtained with mode-locked $3\times\omega$ Nd:YAG laser pulses and nitrogen laser excitation shows significant decline with increasing molecular weight, *M*. Short laser pulses discriminate against analytes of high molecular weight, $M >$ 5000. The solid line represents the sigmoidal fit to guide the eye. Data points represent measurements on the following peptides: L Enk, leucine enkephalin; Ang I, angiotensin I; Sub P, substance P; Ins, bovine insulin; Cyt C, cytochrome C; Lys, lysozyme; SOD, superoxidase dismutase; BSA, bovine serum albumin; and IgG, immunoglobulin G. (b) Ion velocities measured by delayed extraction method as a function of ion mass (from ref 39) show a decline similar to the ion yield ratio data in part a.

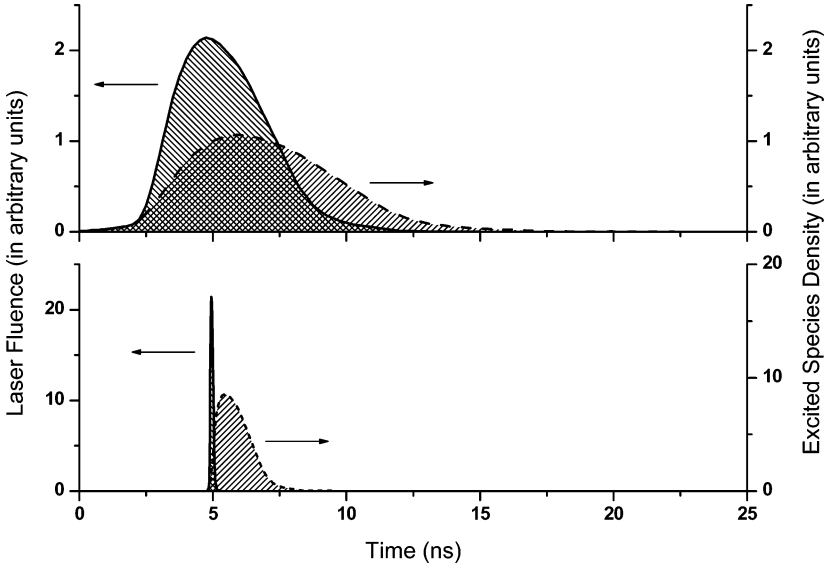

Figure 8. Temporal overlap between laser fluence (solid line) and excited species density (dashed line) for the nanosecond (top panel) and the picosecond laser pulses (bottom panel). Temporal profile of the nanosecond laser pulse was measured with a fast optical detector (DET210, Thorlabs Inc, Newton, NJ). Shape of picosecond pulse was represented by a Gaussian of corresponding width. Excited species density curves are based on the fluorescence lifetime of the excited DHB molecule (from refs 36 and 37) and on the model in ref 6.

Analyte Ion Yield. The variation of total analyte ion yield is used to describe MALDI spectra of leucine enkephalin, angiotensin I, substance P, bovine insulin, cytochrome C, lysozyme, superoxidase dismutase, and bovine serum albumin from DD samples of DHB (not shown). The picosecond laser works as well as the nanosecond laser when analyzing small molecules such as substance P, angiotensin I, and leucine enkephalin. However, for the insulin−DHB system, spot-to-spot reproducibility with the picosecond laser is poor whereas a stable signal is obtained with the nanosecond laser. For proteins with higher molecular weight, the picosecond laser produces marginal analyte signal, whereas with the nanosecond laser spectra are easily obtained. Figure 5 helps to explain why threshold laser fluence is preferred in MALDI experiments with nitrogen laser. When fluence goes significantly above threshold, fewer molecular ions are available, thus decreasing the supply of protonating agents in Scheme 2. Similar to earlier observations made with a femtosecond laser, when the picosecond laser is used there is a dramatic drop in the analyte ion yield at high molecular weights. This finding points out that Scheme 2 and gas dynamic considerations alone cannot fully account for analyte ionization in MALDI, i.e., with the higher yield of $[M + H]^+$ in the plume generated by the picosecond laser, the production of protonated analyte ions is not necessarily more efficient.

The efficiency of ionization by the two lasers can be expressed by the analyte ion yield ratio, Y(ps laser)/Y(ns laser). The molecular weight dependence of the ion yield ratio shows significant decline with increasing molecular weight (see Figure 7a). While small variations in this ratio are observed from peptide to peptide in the middle of the molecular weight range, the general trend is clear from the sigmoidal fit. Above $M >$ 5000 the picosecond laser produces very low ion yield, whereas the nanosecond laser shows much milder decline, thus the ratio falls significantly.

One may consider that in-plume reactions leading to secondary ionization have a direct connection with the laser pulse length. It is expected that the longer pulse can continuously lift off matrix and guest molecules into the gas phase where more plume interactions and photochemical reactions hence ensue. Short pulses, however, eject the molecules into the gas phase during a shorter period and plume interactions and/or proton transfer are not sustained by continuous excitation. Figure 8 is a schematic drawing illustrating the vastly different interaction times between the plume and the pulses of the nanosecond and picosecond lasers. This phenomenon can explain general differences in ion yields between the two lasers but cannot account for the analyte mass dependence shown in Figure 7a.

A possible explanation comes from recent measurements of analyte ion velocities in MALDI.[39] By using the delayed ion extraction method to determine the initial velocities, a significant decline was observed with increasing molecular weight (Figure 7b). Comparing the two panels in Figure 7 over the same molecular weight range reveals a comparable drop of ion yield ratios and initial velocities. Assuming that the ion velocities are similar to the velocities of the neutral molecules, one can infer an increasing difference between the reactant velocities in Scheme 2. The protonated matrix ions can be as much as two times faster than the heavy analyte molecules. As a consequence, the interaction time between these reacting species is limited by the difference in their velocities. The heavier the analyte becomes the shorter time it interacts with the primary ion. The factor of 200 difference in pulse lengths between the two types of laser excitation creates a large difference in the corresponding plume lifetimes. As is clear from Figure 8, the nanosecond laser creates a longer lasting (and spatially more extended) plume than the picosecond laser. When the two reactants in Scheme 2 have different velocities, the interaction times can become dramatically shorter for the picosecond laser. This in turn can lead to the drop of ion yield ratio shown in Figure 7a. In this respect, further temporally resolved 2-pulse or multi-pulse experiments are the probe of choice to explore the fast plume dynamics and to give a more detailed description of ion production in MALDI.

Conclusions

In this report, it is shown that the total ion yield in MALDI is primarily controlled by the laser fluence throughout the nanosecond to the picosecond laser pulse length domain. Matrix molecular ion yields reveal that the nanosecond laser induces significant fragmentation, whereas the picosecond laser produces

predominantly molecular ions. On the basis of these observations an improved photophysical mechanism of MALDI is proposed. By introducing ladder switching to fragment channels in addition to ladder climbing and exciton pooling, this new model can account for a more realistic diversity of ions, including matrix fragments and analyte−fragment ion adducts.

We have also demonstrated that ionization threshold is affected by sample morphology. Fractal coarsening of the pellet surface induced by increasing the compacting pressure results in an elevated primary ion formation threshold in MALDI. This surface morphology effect needs to be incorporated in future quantitative descriptions of the MALDI ion yield. A similar fractal coarsening phenomenon is expected to occur during multiple laser exposure of particular spots on the sample surface. This process could account for the local depletion of MALDI signal.

Very importantly, subnanosecond excitation results in a limited mass detection range. The remarkable decline of analyte ion production with increasing mass for picosecond laser excitation is rationalized in terms of the reduced interaction time between the matrix and analyte species due to differences in their velocity. In this model, the light primary matrix ions outrun the heavy analyte molecules in the expanding plume. The shorter ion generation time of the picosecond laser greatly exacerbates this effect.

Acknowledgment. Financial support from the National Science Foundation (CHE-9873610) and the Department of Energy (DE-FG02-01ER15129) is appreciated. DOE's support does not constitute an endorsement by DOE of the views expressed in the article. Special thanks are due to Dr. Walter F. Rowe of The George Washington University for helping to acquire the SEM images, to Dr. Jonas Kolenda of EKSPLA for reconfiguring the laser at reduced repetition rate, to Ioan Marginean of The George Washington University for writing the data acquisition program, and to Martin Nezadal and Oldrich Zmeskal of Brno University of Technology for generously providing the fractal analysis package.

References and Notes

(1) Tanaka, K.; Waki, H.; Ido, Y.; Akita, S.; Yoshida, Y.; Yoshida, T. *Rapid Commun. Mass Spectrom.* **1988**, *2*, 151.
(2) Karas, M.; Hillenkamp, F. *Anal. Chem.* **1988**, *60*, 2299.
(3) Dreisewerd, K. *Chem. Rev.* **2003**, *103*, 395.
(4) Allwood, D.; Dreyfus, R.; Perera, I.; Dyer, P. *Appl. Surf. Sci.* **1997**, *109/110*, 154.
(5) Allwood, D.; Dyer, P. *Chem. Phys.* **2000**, *261*, 457.
(6) Knochenmuss, R. *J. Mass. Spectrom.* **2002**, *37*, 867.
(7) Knochenmuss, R. *Anal. Chem.* **2003**, *75*, 2199.
(8) Tang, X.; Sadeghi, M.; Olumee, Z.; Vertes, A. *Rapid Commun. Mass Spectrom.* **1997**, *11*, 484.
(9) Knochenmuss, R.; Vertes, A. *J. Phys. Chem. B* **2000**, *104*, 5406.
(10) Moskovets, E.; Vertes, A. *J. Phys. Chem. B* **2002**, *106*, 3301.
(11) Zenobi, R.; Knochenmuss, R. *Mass Spectrom. Rev.* **1998**, *17*, 337.
(12) Cherier, M.; Cotter, R. *Rapid Commun. Mass Spectrom.* **1991**, *5*, 611.
(13) Beavis, R.; Chaudhary, T.; Chait, B. *Org. Mass Spectrom.* **1992**, *27*, 156.
(14) Demirev, P.; Westman, A.; Reimann, C.; Hakansson, P.; Barofsky, D.; Sundqvist, B.; Cheng, Y.; Seibt, W. *Rapid Commun. Mass Spectrom.* **1992**, *6*, 187.
(15) Johnson, R. *Int. J. Mass Spectrom. Ion Processes* **1994**, *139*, 25.
(16) Dreisewerd, K.; Schurenberg, M.; Karas, M.; Hillenkamp, F. *Int. J. Mass Spectrom. Ion Processes* **1996**, *154*, 171.
(17) Papantonakis, M.; Kim, J.; Hess, W.; Haglund, R. *J. Mass Spectrom.* **2002**, *37*, 639.
(18) Dietz, W.; Neusser, H.; Boesl, U.; Schlag, E.; Lin, S. *Chem. Phys.* **1982**, *66*, 105.
(19) Gobeli, D.; Yang, J.; El-Sayed, M. *Chem. Rev.* **1985**, *85*, 529.
(20) Vertes, A.; Irinyi, G.; Gijbels, R. *Anal. Chem.* **1993**, *65*, 2389.
(21) Bencsura, A.; Vertes, A. *Chem. Phys. Lett.* **1995**, *247*, 142.
(22) Zhigilei, L.; Kodali, P.; Garrison, B. *J. Phys. Chem. B* **1997**, *101*, 2028.
(23) Wu, X.; Sadeghi, M.; Vertes, A. *J. Phys. Chem. B* **1998**, *102*, 4770.
(24) Zhigilei, L.; Garrison, B. *Rapid Comm. Mass Spectrom.* **1998**, *12*, 1273.
(25) Zhigilei, L.; Garrison, B. *Appl. Surf. Sci.* **1998**, *127−129*, 142.
(26) Sadeghi, M.; Wu, X.; Vertes, A. *J. Phys. Chem. B* **2001**, *105*, 2578.
(27) Westman, A.; Huth-Fehre, T.; Demirev, P.; Sundqvist, U. R. *J. Mass Spectrom.* **1995**, *30*, 206.
(28) Alwood, D. A.; Perera, I. K.; Perkins, J.; Dyer, P. E.; Oldershaw, G. *Appl. Surf. Sci.* **1996**, *103*, 231.
(29) Sadeghi, M.; Vertes, A. *Appl. Surf. Sci.* **1998**, *127−129*, 226.
(30) Olumee, Z.; Sadeghi, M.; Tang, X.; Vertes, A. *Rapid Commun. Mass Spectrom.* **1995**, *9*, 744.
(31) Ehring, H.; Karas, M.; Hillenkamp, F. *Org. Mass. Spectrom.* **1992**, *27*, 472.
(32) Dreisewerd, K.; Schurenberg, M.; Karas, M.; Hillenkamp, F. *Int. J. Mass Spectrom. Ion Processes* **1995**, *141*, 127.
(33) Mickeleit, M. *J. Am. Ceram. Soc.* **1987**, *70*, C-387.
(34) Karbach, V.; Knochenmuss, R. *Rapid Commun. Mass Spectrom.* **1998**, *12*, 968.
(35) Lin, Q.; Knochenmuss, R. *Rapid Commun. Mass Spectrom.* **2001**, *15*, 1422.
(36) Allwood, D.; Dyer, P.; Dreyfus, R. *Rapid Commun. Mass Spectrom.* **1997**, *11*, 499.
(37) Ludemann, H.; Redmond, R.; Hillenkamp, F. *Rapid Commun. Mass Spectrom.* **2002**, *16*, 1287.
(38) Luo, G.; Marginean, I.; Vertes, A. *Anal. Chem.* **2002**, *74*, 6185.
(39) Berkenkamp, S.; Menzel, C.; Hillenkamp, F.; Dreisewerd, K. *J. Am. Soc. Mass Spectrom.* **2002**, *13*, 209.